



# Discovery of the soft electronic modes of the trimeron order in magnetite

Edoardo Baldini<sup>® 1,10</sup>, Carina A. Belvin<sup>® 1,10</sup>, Martin Rodriguez-Vega<sup>2,3</sup>,
Ilkem Ozge Ozel<sup>1</sup>, Dominik Legut<sup>4</sup>, Andrzej Kozłowski<sup>5</sup>, Andrzej M. Oleś<sup>® 6,7</sup>, Krzysztof Parlinski<sup>® 8</sup>,
Przemysław Piekarz<sup>8</sup>, José Lorenzana<sup>® 9</sup>, Gregory A. Fiete<sup>1,3</sup> and Nuh Gedik<sup>® 1 ⋈</sup>

The Verwey transition in magnetite (Fe<sub>2</sub>O<sub>4</sub>) is the first metalinsulator transition ever observed1 and involves a concomitant structural rearrangement and charge-orbital ordering. Owing to the complex interplay of these intertwined degrees of freedom, a complete characterization of the low-temperature phase of magnetite and the mechanism driving the transition have long remained elusive. It was demonstrated in recent years that the fundamental building blocks of the charge-ordered structure are three-site small polarons called trimerons2. However, electronic collective modes of this trimeron order have not been detected to date, and thus an understanding of the dynamics of the Verwey transition from an electronic point of view is still lacking. Here, we discover spectroscopic signatures of the low-energy electronic excitations of the trimeron network using terahertz light. By driving these modes coherently with an ultrashort laser pulse, we reveal their critical softening and hence demonstrate their direct involvement in the Verwey transition. These findings shed new light on the cooperative mechanism at the origin of magnetite's exotic ground state.

Along with his groundbreaking discovery in 1939, Verwey postulated the emergence of a charge ordering of Fe²+ and Fe³+ ions as the mechanism driving the dramatic conductivity drop at  $T_{\rm V} \approx 125\,\rm K$  (ref.¹). A vast number of subsequent experimental and theoretical investigations, including those by Anderson³, Mott⁴ and many others, have stimulated a still unresolved debate over a complete description of the Verwey transition⁵.6. In particular, several seemingly incompatible findings related to the intricate low-temperature phase of magnetite have been reported: the crucial role of Coulomb repulsion⁵, the necessity of including electron–phonon coupling⁴.8,9, small charge disproportionation⁵.10,11, anomalous phonon broadening with the absence of a softening towards  $T_{\rm V}$  (ref.¹²) and the observation of structural fluctuations that are connected to the Fermi surface nesting¹³ and that persist up to the Curie transition temperature ( $T_{\rm C} \approx 850\,\rm K)$ ¹⁴.

The last decade witnessed significant progress in understanding the Verwey transition from a structural point of view. Most notably, a refinement of the low-temperature charge-ordered structure as a network of three-site small polarons, termed trimerons, was given by X-ray diffraction<sup>2</sup> (Fig. 1a). A trimeron consists of a linear unit of three Fe sites accompanied by distortions of the two outer Fe<sup>3+</sup>

ions towards the central Fe<sup>2+</sup> ion. An orbital ordering of coplanar  $t_{2g}$  orbitals is also established on each ion within the trimeron (Fig. 1b). This picture of the trimeron order has been crucial for determining the correct noncentrosymmetric Cc space group of magnetite and explaining its spontaneous charge-driven ferroelectric polarization<sup>2,6,15</sup>. Nevertheless, despite extensive research, no soft modes of the trimeron order have been detected to date. Unveiling novel types of collective modes in the low-temperature phase of magnetite and their critical softening would significantly shape our understanding of the long-sought cooperative phenomenon at the origin of the Verwey transition.

Here, we use time-domain terahertz spectroscopy (Fig. 1c) to reveal the electronic modes of the trimeron order. Their signature is imprinted on the equilibrium optical conductivity of the material in an energy-temperature range previously unexplored. We establish their involvement in the Verwey transition by driving them coherently with an ultrashort near-infrared laser pulse and mapping their softening with a delayed terahertz probe. We propose a model of coherent polaron tunnelling to describe the nature of these trimeron excitations

Figure 2a shows the real part of the low-energy optical conductivity  $(\sigma_1)$  measured in equilibrium on a magnetite single crystal. Slightly below  $T_{v}$ , the spectrum displays a broad, featureless continuum (red curve), which previous studies attributed to a powerlaw behaviour expected in the presence of charge hopping between polaronic states<sup>16</sup>. As the temperature is lowered well below  $T_{\rm v}$  to a hitherto unexplored regime (pink and blue curves), the continuum in the optical conductivity is suppressed and two Lorentzian lineshapes clearly emerge. These excitations slightly harden with decreasing temperature and are centred around 1.5 and 4.2 meV at 7 K. Since they appear below the charge gap for single-particle excitations<sup>17</sup>, it is natural to ascribe them to distinct low-energy collective modes at the Brillouin zone centre. Intriguingly, these excitations have never been observed in any previous study on magnetite<sup>16,18-22</sup>. Thus, it is pivotal to identify their origin and clarify their potential involvement in the Verwey transition.

We make use of advanced density functional theory (DFT) calculations of the phonon dispersion curves in the low-temperature Cc symmetry of magnetite to compare the energy of the two observed excitations with that of long-wavelength lattice modes (see Methods and Extended Data Fig. 1a). The lowest-lying optical

<sup>1</sup>Department of Physics, Massachusetts Institute of Technology, Cambridge, MA, USA. <sup>2</sup>Department of Physics, The University of Texas at Austin, Austin, TX, USA. <sup>3</sup>Department of Physics, Northeastern University, Boston, MA, USA. <sup>4</sup>IT4Innovations Center, VSB-Technical University of Ostrava, Ostrava, Czech Republic. <sup>5</sup>Faculty of Physics and Applied Computer Science, AGH-University of Science and Technology, Kraków, Poland. <sup>6</sup>Marian Smoluchowski Institute of Physics, Jagiellonian University, Kraków, Poland. <sup>7</sup>Max Planck Institute for Solid State Research, Stuttgart, Germany. <sup>8</sup>Institute of Nuclear Physics, Polish Academy of Sciences, Kraków, Poland. <sup>9</sup>Institute for Complex Systems, National Research Council and Department of Physics, University of Rome La Sapienza, Rome, Italy. <sup>10</sup>These authors contributed equally: Edoardo Baldini, Carina A. Belvin. <sup>∞</sup>e-mail: gedik@mit.edu

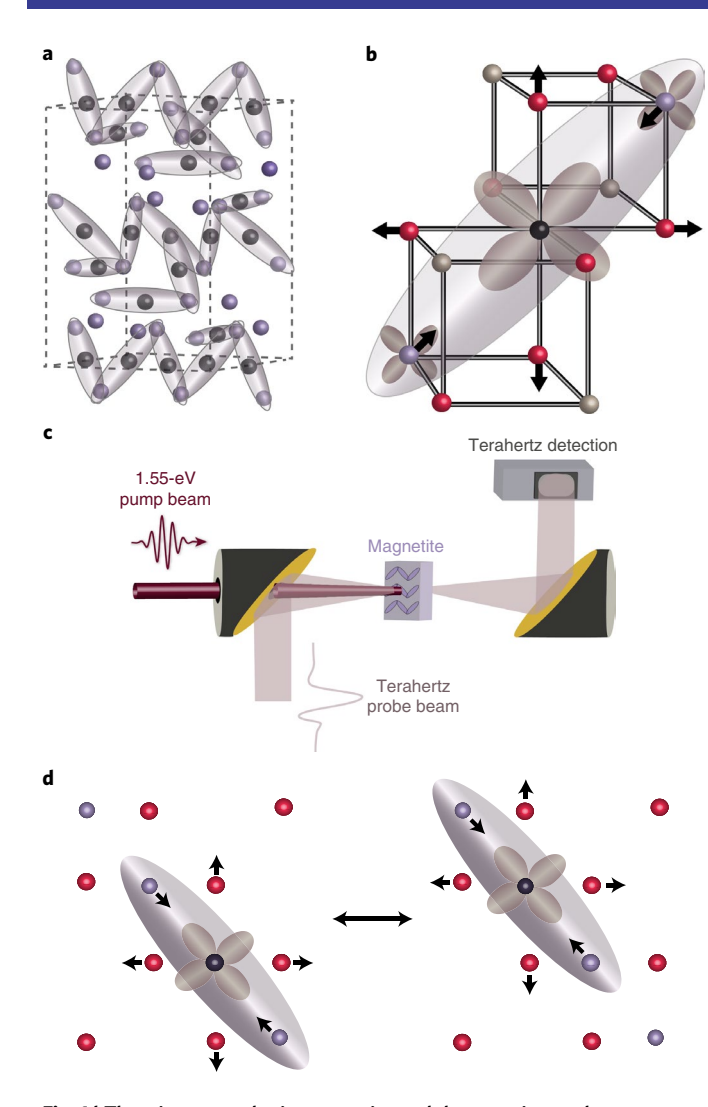


Fig. 1 | The trimeron order in magnetite and the experimental methodology. a, The low-temperature charge-ordered structure of magnetite as a network of trimerons, small polarons that extend over three linear Fe sites. The purple and black spheres represent  $Fe^{3+}$  and  $Fe^{2+}$ ions, respectively. **b**, Each trimeron consists of two outer Fe<sup>3+</sup> ions and one central Fe<sup>2+</sup> ion (the arrows depict distortions of the lattice). This charge ordering is accompanied by an ordering of coplanar  $t_{2g}$  orbitals on each Fe site within the trimeron. The surrounding oxygen ions are shown in red, and the grey spheres represent Fe sites that do not participate in the trimeron. c, A schematic of the experimental set-up. Time-domain terahertz spectroscopy in a transmission geometry is used to determine the lowenergy optical conductivity of the sample in equilibrium (without the pump beam). To examine its dynamics, an ultrashort near-infrared (1.55 eV) pump pulse sets the system out of equilibrium and a weak, delayed terahertz probe pulse measures the pump-induced change in the optical conductivity. **d**, A schematic depicting the trimeron sliding motion resulting from the coherent polaron tunnelling between an Fe<sup>2+</sup> site and a neighbouring Fe<sup>3+</sup> site. Figure adapted with permission from: **a.b.** ref. <sup>2</sup>. Springer Nature Ltd.

phonons at the  $\Gamma$  point of the Brillouin zone have symmetries A' and A' and correspond to the folded  $\Delta_5$  mode of the cubic phase. As shown in Extended Data Fig. 1a, their energy of 8 meV is in excellent agreement with inelastic neutron<sup>19,23</sup> and X-ray<sup>12</sup> scattering data. Therefore, the low-energy modes in our experiment cannot be assigned to phonons. Similarly, the magnon dispersion curves measured by inelastic neutron scattering do not show any

long-wavelength spin waves with energies in our spectral range  $^{18}$ . Since ferrimagnetism in magnetite is quite robust (with  $T_{\rm C} \approx 850\,\rm K$ ), these excitations would be expected to persist at high temperature  $^{16}$ . Thus, after ruling out these scenarios of conventional types of collective modes (see Supplementary Note 1 for additional details), the only remaining possibility is that the detected modes are collective excitations of the trimeron order.

We now clarify whether these collective modes play a key role in the Verwey transition by unravelling their critical behaviour. This is a challenging task to accomplish under equilibrium conditions, as the broad conductivity continuum seen in Fig. 2a obscures any spectroscopic signatures of the collective modes at temperatures proximate to  $T_{v}$ . It is thus unclear whether the modes persist as strongly damped Lorentzians buried under this continuum and how their peak energies change with temperature. To overcome this experimental difficulty, we illuminate our magnetite crystal with an ultrashort near-infrared laser pulse and drive its collective modes coherently24. We vary the laser fluence absorbed by our sample, exploring a regime that allows us to transiently increase the lattice temperature but not completely melt the trimeron order<sup>25,26</sup> (see Supplementary Note 4). We then monitor the fingerprint of the coherently excited collective modes on the low-energy electrodynamics of the system.

Figure 2b shows the pump-induced change in the terahertz electric field ( $\Delta E$ ) through the sample over a range of absorbed fluences. As a function of pump-probe delay, we observe prominent oscillations that are signatures of collective modes coherently evolving in time. On closer examination, these oscillations cannot be described by a single frequency, but rather by two frequencies, which indicates the presence of two distinct coherent excitations (see Supplementary Note 5B). Fitting the time-domain traces to the simplest model (consisting of two damped sine waves) reveals that at the lowest fluence the modes have energies very close to those present in the equilibrium conductivity at 7 K and therefore are the same excitations. Slight deviations in their energies relative to equilibrium possibly occur due to the non-thermal action of the pump pulse during photoexcitation. Their simultaneous presence in the frequency domain (as dipole-allowed modes) and in the time domain (as Raman-active modes) is naturally explained by the breakdown of the selection rules for infrared and Raman activity in the noncentrosymmetric Cc crystal structure of magnetite<sup>2</sup>. The two modes display a significant dependence on pump fluence. In particular, their energies soften dramatically towards the critical fluence  $(F_C)$  identified in previous studies<sup>25,26</sup> (Fig. 2c). This behaviour strikingly establishes their active involvement in the Verwey transition. In addition, the mode amplitudes first rise linearly until  $\sim 1 \, \text{mJ cm}^{-2}$ and then dramatically drop in the proximity of  $F_c$  (Fig. 2d), confirming the scenario of an impulsive Raman generation mechanism<sup>24</sup> that gets destabilized at higher fluences when the Verwey transition is approached due to transient lattice heating<sup>27,28</sup>.

Finally, we establish whether the newly discovered collective excitations mutually interact. This is achieved by resolving the spectral region of the low-energy conductivity in which each coherent mode resonates. Figure 3a shows the spectro-temporal evolution of the differential optical conductivity ( $\Delta \sigma_1$ ) following photoexcitation. We observe the emergence of two broad features centred around 2 and 3 meV, which indicate how the lineshapes of the two modes in equilibrium are modified by the presence of the pump pulse. The shape and sign of the differential signal suggests that the main effect of this modulation is a broadening of the equilibrium Lorentzian lineshapes together with their amplitude change, although the exact form of the change is difficult to determine owing to the complexity of this material system. We then select a temporal trace at a representative terahertz photon energy (Fig. 3b) and perform a Fourier transform analysis (Fig. 3c). This yields the frequencies of the two collective modes expected from Fig. 2a-c. Iterating this procedure

NATURE PHYSICS LETTERS

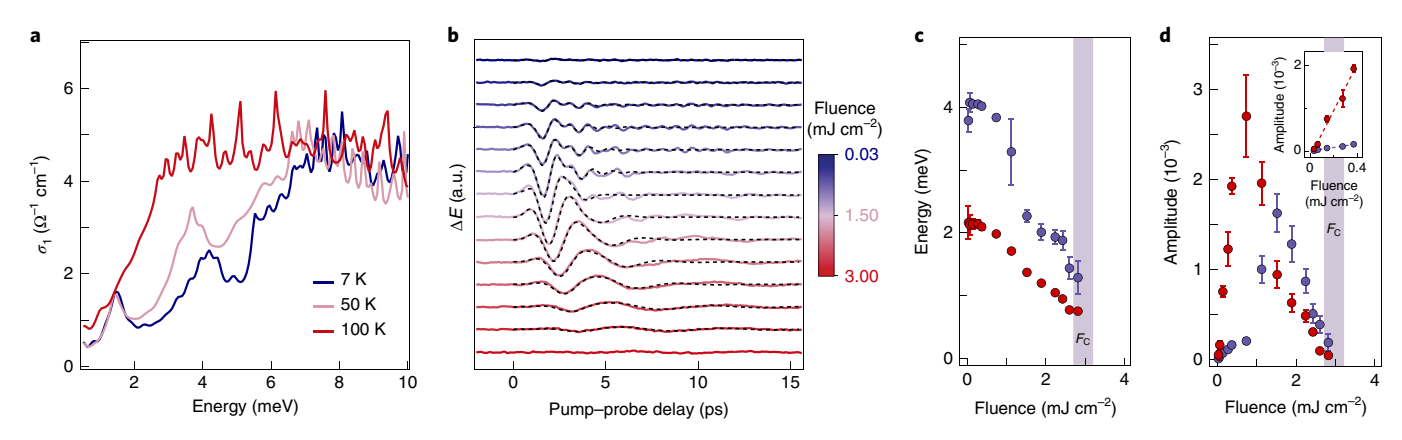


**Fig. 2** | Observation of low-energy electronic collective modes and their critical softening. **a**, The real part of the equilibrium optical conductivity ( $\sigma_1$ ) of magnetite in the terahertz region. The spectrum near  $T_v$  (red curve) exhibits a broad, featureless continuum that rises with a power-law behaviour, in accordance with a previous report<sup>16</sup>. Lowering the temperature reveals two Lorentzian lineshapes (pink and blue curves) that are due to collective modes. **b**, The pump-induced change in the terahertz electric field ( $\Delta E$ ) transmitted through the sample at 7 K following photoexcitation with a near-infrared (1.55 eV) pump pulse at various absorbed fluences. The traces are offset vertically for clarity. Each curve was fitted to two damped sine waves and the fits in the time domain are displayed as dashed black lines. **c**, The energy of each oscillation extracted from the fits as a function of fluence. At low fluence, the energies are close to those in **a** at 7 K, so the oscillations correspond to the same collective modes present in equilibrium. Both energies soften with increasing fluence, demonstrating their involvement in the Verwey transition. **d**, The amplitude of each mode versus fluence. The inset shows the linear rise of the amplitudes in the low-fluence regime, which is compatible with an impulsive Raman excitation process. The shaded bars in **c** and **d** indicate the critical fluence for melting the trimeron order as reported in refs. <sup>25,26</sup>. The error bars in **c** and **d** represent the 95% confidence interval for the corresponding fit parameters.

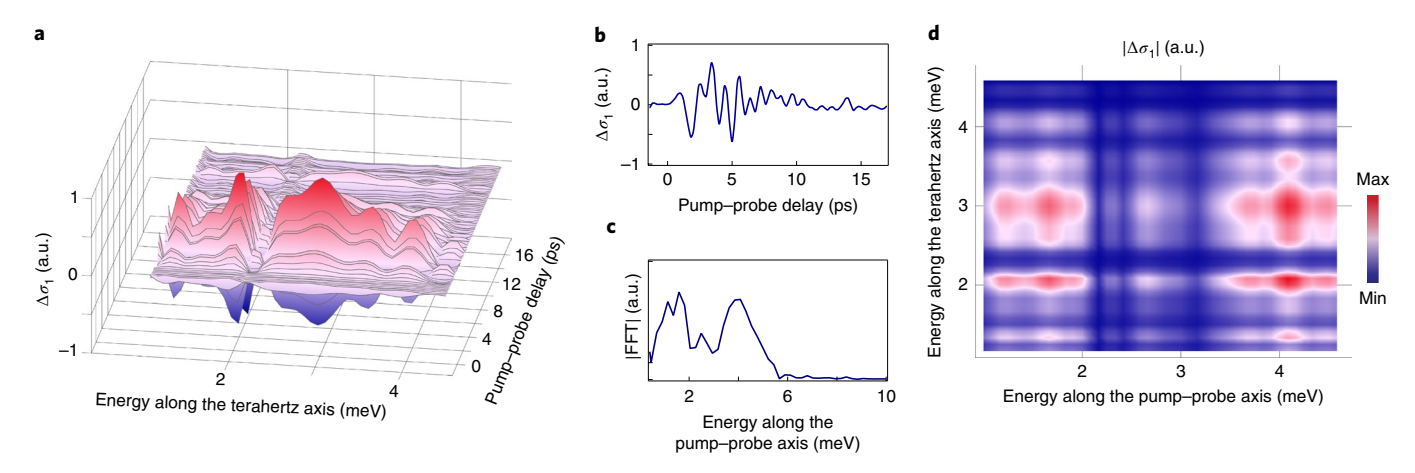


**Fig. 3 | Mutual coupling between the two collective modes. a**, The spectro-temporal evolution of the photoinduced change in the real part of the optical conductivity ( $\Delta\sigma_1$ ) in the terahertz range following photoexcitation with a near-infrared (1.55 eV) pump pulse. The temperature is 7 K and the absorbed fluence is 0.27 mJ cm<sup>-2</sup>. Two broad features are observed around 2 and 3 meV and they are coherently modulated as a function of pump-probe delay. **b**, A trace of  $\Delta\sigma_1$  as a function of pump-probe delay at a representative terahertz photon energy. **c**, A Fourier transform of the temporal trace shown in **b**, which reveals two distinct peaks corresponding to the two coherent collective modes (compare their energies with Fig. 2a,c). **d**, The amplitude of the Fourier transform taken along the pump-probe delay axis at each terahertz photon energy of the map shown in **a**. We observe that two peaks are present in the Fourier transform at each photon energy, which indicates that the two electronic modes are coupled to each other.

at all terahertz photon energies (Fig. 3d) reveals that the entire spectrum is modulated by both coherent electronic modes, demonstrating that these two modes are coupled to one another.

To rationalize the behaviour of these coherent collective modes after photoexcitation, we develop the simplest time-dependent Ginzburg–Landau (GL) model compatible with the symmetries of the system. In our calculations, we consider electronic collective mode fluctuations described by a complex order parameter  $\psi = |\psi| e^{i\varphi}$ . In the GL potential  $F = F[\psi]$ , we include a nonlinear term arising from electronic interactions, a linear coupling term between the real and imaginary parts of  $\psi$  responsible for inversion symmetry

breaking and a pinning potential arising from impurity effects. The non-equilibrium action of the pump pulse on the mode fluctuations is introduced through a coupling to the intensity of the pump electric field. The full dynamics of the system are described by equations of motion that include phenomenological relaxation and inertial terms for both  $|\psi|$  and  $\varphi$  (see Methods). Despite its simplicity, our model captures the salient features of our experimental data. Specifically, the energies of both  $|\psi|$  and  $\varphi$  soften towards  $F_{\rm C}$  (Fig. 4a) and the oscillation amplitudes of the modes rise linearly with increasing fluence before experiencing a dramatic quench in the proximity of  $F_{\rm C}$  (Fig. 4b). Furthermore, there is a crossing of

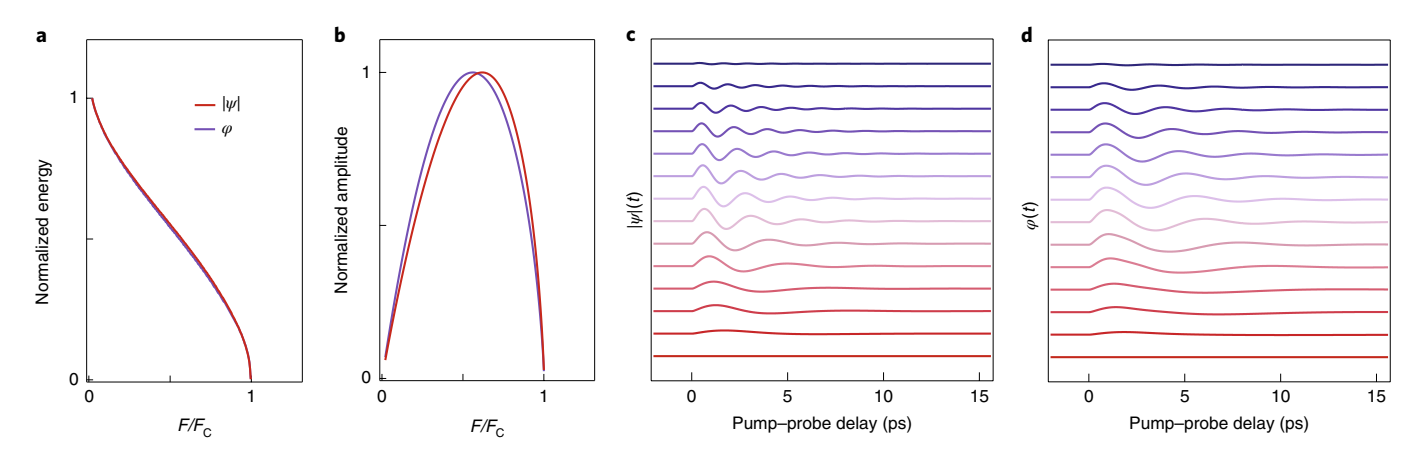


**Fig. 4** | The time-dependent **GL** theory describing the dynamics of the collective modes. **a,b**, The dependence of the energies (**a**) and amplitudes (**b**) of both components of the order parameter ( $|\psi|$  and  $\varphi$ ) as a function of pump fluence. **c,d**, The evolution of  $|\psi|(t)$  (**c**) and  $\varphi(t)$  (**d**) in the time domain over a range of fluences. The calculated behaviour matches the qualitative trends observed in the experiments (see Fig. 2b-d), namely the softening of the energies and the initial linear increase in the amplitudes followed by their destabilization towards the critical fluence  $F_c$ .

the amplitudes of the modes around  $0.5F_{\rm C}$ , which is also present in the experimental data (see Fig. 2d). The resulting time dependences of  $|\psi|$  and  $\varphi$  are plotted in Fig. 4c,d, respectively, for several fluence values. While our model successfully reproduces the qualitative behaviour of the experimentally observed dynamics, some quantitative mismatch is still present. In particular, deviation from the observed quasi-mean-field behaviour of the mode energies in Fig. 2c is due to the exact energy-fluence functional form used to describe the thermodynamic properties of the material.

Our results are rather surprising given the current understanding of magnetite's low-temperature phase. Since in this material the charge order is commensurate with the lattice and the Verwey transition is thought to be of an order-disorder type on the basis of the observation of overdamped (that is, diffusive) modes<sup>13,21,29,30</sup>, the detection of underdamped (and therefore propagating) soft electronic modes is unexpected. This apparent contradiction can be reconciled by recalling that the trimeron order in magnetite leads to the development of a spontaneous ferroelectric polarization<sup>2,6,15</sup>. The ferroelectric instability is of the electronic (improper) type and involves charges that are weakly bound to the underlying lattice6. Low-energy modes can naturally emerge as collective fluctuations of charges within the trimeron network on top of the robust commensurate charge order. Although our observed modes seem reminiscent of the electronic component of amplitudons and phasons in conventional charge-density wave systems, such a simplified picture is not expected to capture the complexity of the trimeron order in magnetite. Here, we propose that these excitations can be described by oscillations of the trimeron network using a model of coherent polaron tunnelling. In our calculations, we consider a quantum tunnelling process involving self-trapped carriers on the central Fe2+ sites of the trimerons and we compute the potential energy barrier for their coherent hopping to outer Fe<sup>3+</sup> sites using DFT<sup>15</sup>. By estimating the bonding-antibonding splitting arising from the superposition of the two states created by tunnelling through the barrier, we find that its energy lies around 5 meV (that is, within the monitored terahertz range; see Supplementary Note 1D). As shown schematically in Fig. 1d, this coherent polaron oscillation corresponds to a sliding mode of the trimeron along its long axis. In analogy with nematicity, such motion is expected to create a smaller disturbance of the trimeron order compared to other alternatives such as the rotation of the  $t_{2g}$  orbital participating in the trimeron (see Supplementary Note 1C for a DFT analysis of a scenario involving this type of orbiton). While at low temperature this energy splitting is robust and allows for coherent tunnelling, as the temperature increases the polaron motion becomes overdamped, broadening the levels and reducing their relative splitting. As a result, the excitations soften with increasing temperature towards  $T_{\rm V}$  and are no longer supported in the absence of the trimeron order. We believe that only the development of advanced theoretical models will contribute to the identification of the real-space charge distribution characterizing these collective fluctuations. Indeed, their extremely low energy and small atomic displacements hinder their investigation with other steady-state<sup>20,22</sup> and time-resolved<sup>25,31,32</sup> probes of charge/structural dynamics (see Supplementary Note 2). In contrast, our optical pump–terahertz probe approach enables the detection of these low-energy coherent modes with unprecedented sensitivity.

The current study highlights the strength of ultrafast terahertz probes in uncovering the soft character of electronic collective modes associated with an intricate order, in line with recent experiments on the Higgs and Leggett modes in superconductors<sup>33,34</sup>. Beyond these results, we envision using strong terahertz fields<sup>35</sup> to resonantly drive the modes of the trimeron order in magnetite and similar charge-ordered compounds, enabling the coherent control of electronic ferroelectricity.

#### Online content

Any methods, additional references, Nature Research reporting summaries, source data, extended data, supplementary information, acknowledgements, peer review information; details of author contributions and competing interests; and statements of data and code availability are available at <a href="https://doi.org/10.1038/s41567-020-0823-y">https://doi.org/10.1038/s41567-020-0823-y</a>.

Received: 24 September 2019; Accepted: 2 February 2020; Published online: 9 March 2020

# References

- Verwey, E. J. W. Electronic conduction of magnetite (Fe<sub>3</sub>O<sub>4</sub>) and its transition point at low temperatures. *Nature* 144, 327–328 (1939).
- Senn, M. S., Wright, J. P. & Attfield, J. P. Charge order and three-site distortions in the Verwey structure of magnetite. *Nature* 481, 173–176 (2012).
- Anderson, P. W. Ordering and antiferromagnetism in ferrites. Phys. Rev. 102, 1008–1013 (1956).
- Mott, N. F. Materials with mixed valency that show a Verwey transition. Philos. Mag. B 42, 327–335 (1980).
- Walz, F. The Verwey transition a topical review. J. Phys. Cond. Matter 14, R285–R340 (2002).
- 6. Khomskii, D. I. Transition Metal Compounds. (Cambridge Univ. Press, 2014).

NATURE PHYSICS LETTERS

- Leonov, I., Yaresko, A. N., Antonov, V. N., Korotin, M. A. & Anisimov, V. I. Charge and orbital order in Fe<sub>3</sub>O<sub>4</sub>. Phys. Rev. Lett. 93, 146404 (2004).
- Yamada, Y. Molecular polarons and valence fluctuations in Fe<sub>3</sub>O<sub>4</sub>. *Philos. Mag. B* 42, 377–385 (1980).
- 9. Piekarz, P., Parlinski, K. & Oleś, A. M. Mechanism of the Verwey transition in magnetite. *Phys. Rev. Lett.* **97**, 156402 (2006).
- Wright, J. P., Attfield, J. P. & Radaelli, P. G. Long range charge ordering in magnetite below the Verwey transition. *Phys. Rev. Lett.* 87, 266401 (2001).
- 11. Subías, G. et al. Structural distortion, charge modulation and local anisotropies in magnetite below the Verwey transition using resonant x-ray scattering. *J. Synchrotron Rad.* **19**, 159–173 (2012).
- 12. Hoesch, M. et al. Anharmonicity due to electron–phonon coupling in magnetite. *Phys. Rev. Lett.* **110**, 207204 (2013).
- Bosak, A. et al. Short-range correlations in magnetite above the Verwey temperature. Phys. Rev. X 4, 011040 (2014).
- 14. Perversi, G. et al. Co-emergence of magnetic order and structural fluctuations in magnetite. *Nat. Commun.* **10**, 2857 (2019).
- Yamauchi, K., Fukushima, T. & Picozzi, S. Ferroelectricity in multiferroic magnetite Fe<sub>3</sub>O<sub>4</sub> driven by noncentrosymmetric Fe<sup>2+</sup>/Fe<sup>3+</sup> charge-ordering: first-principles study. *Phys. Rev. B* 79, 212404 (2009).
- Pimenov, A. et al. Terahertz conductivity at the Verwey transition in magnetite. *Phys. Rev. B* 72, 035131 (2005).
- Gasparov, L. V. et al. Infrared and Raman studies of the Verwey transition in magnetite. *Phys. Rev. B* 62, 7939–7944 (2000).
- McQueeney, R. J. et al. Influence of the Verwey transition on the spin-wave dispersion of magnetite. J. Appl. Phys. 97, 10A902 (2005).
- Borroni, S. et al. Mapping the lattice dynamical anomaly of the order parameters across the Verwey transition in magnetite. *New J. Phys.* 19, 103013 (2017).
- Huang, H. Y. et al. Jahn–Teller distortion driven magnetic polarons in magnetite. *Nat. Commun.* 8, 15929 (2017).
- Borroni, S. et al. Light scattering from the critical modes of the Verwey transition in magnetite. *Phys. Rev. B* 98, 184301 (2018).
- Elnaggar, H. et al. Magnetic contrast at spin-flip excitations: an advanced x-ray spectroscopy tool to study magnetic-ordering. ACS Appl. Mater. Interfaces 11, 36213–36220 (2019).

- Samuelsen, E. J. & Steinsvoll, O. Low-energy phonons in magnetite. *Phys. Status Solidi B* 61, 615–620 (1974).
- 24. Stevens, T. E., Kuhl, J. & Merlin, R. Coherent phonon generation and the two stimulated Raman tensors. *Phys. Rev. B* **65**, 144304 (2002).
- De Jong, S. et al. Speed limit of the insulator-metal transition in magnetite. Nat. Mater. 12, 882–886 (2013).
- Randi, F. et al. Phase separation in the nonequilibrium Verwey transition in magnetite. Phys. Rev. B 93, 054305 (2016).
- Wall, S. et al. Ultrafast changes in lattice symmetry probed by coherent phonons. *Nat. Commun.* 3, 721 (2012).
- Schaefer, H., Kabanov, V. V. & Demsar, J. Collective modes in quasi-onedimensional charge-density wave systems probed by femtosecond timeresolved optical studies. *Phys. Rev. B* 89, 045106 (2014).
- Yamada, Y., Wakabayashi, N. & Nicklow, R. M. Neutron diffuse scattering in magnetite due to molecular polarons. *Phys. Rev. B* 21, 4642–4648 (1980).
- Borroni, S. et al. Coherent generation of symmetry-forbidden phonons by light-induced electron-phonon interactions in magnetite. *Phys. Rev. B* 96, 104308 (2017).
- 31. Pontius, N. et al. Time-resolved resonant soft x-ray diffraction with free-electron lasers: femtosecond dynamics across the Verwey transition in magnetite. *Appl. Phys. Lett.* **98**, 182504 (2011).
- 32. Pennacchio, F. Spatio-Temporal Observation of Dynamical Structures in Order-Disorder Phenomena and Phase Transitions via Ultrafast Electron Diffraction. PhD thesis, EPFL (2018).
- Matsunaga, R. et al. Light-induced collective pseudospin precession resonating with Higgs mode in a superconductor. *Science* 345, 1145–1149 (2014).
- 34. Giorgianni, F. et al. Leggett mode controlled by light pulses. *Nat. Phys.* 15, 341-346 (2019).
- Kampfrath, T., Tanaka, K. & Nelson, K. A. Resonant and nonresonant control over matter and light by intense terahertz transients. *Nat. Photon.* 7, 680–690 (2013).

**Publisher's note** Springer Nature remains neutral with regard to jurisdictional claims in published maps and institutional affiliations.

© The Author(s), under exclusive licence to Springer Nature Limited 2020

### Methods

Single-crystal growth and characterization. A single crystal of synthetic magnetite oriented in the (111) direction with a thickness of 0.5 mm was used in all experiments. The crystal was grown using the skull melting technique from 99.999% purity Fe<sub>2</sub>O<sub>3</sub>. Afterwards, the crystal was annealed under a CO/CO, gas mixture to establish the appropriate iron/oxygen ratio. The quality and stoichiometry of the sample was characterized by measuring the a.c. magnetic susceptibility to determine the value of  $T_v$ . Supplementary Fig. 1 shows the real part of the a.c. magnetic susceptibility  $\chi'$  as a function of temperature from 117 K to 126 K. The sudden decrease in  $\chi'$  around 123 K indicates that  $T_{\rm v} \approx$  123 K for this sample. This drop in the susceptibility results from microtwinning of the crystal when it undergoes its structural transition from cubic to monoclinic at  $T_{v}$ . In the low-temperature monoclinic phase, the ferroelastic domains constrain the motion of magnetic domain walls due to a higher cost in elastic energy. Consequently, the value of  $\chi'$  should be lower in the monoclinic phase compared to the cubic phase<sup>36</sup>. The temperature at which  $\chi'$  exhibits this discontinuity therefore corresponds to  $T_{v_{\bullet}}$ 

**Time-domain and ultrafast terahertz spectroscopy.** A Ti:sapphire regenerative amplifier system with 100-fs pulses at a photon energy of 1.55 eV and a repetition rate of 5 kHz was used to generate terahertz pulses via optical rectification in a ZnTe crystal. The terahertz signal transmitted through the sample was detected by electro-optic sampling in a second ZnTe crystal with a 1.55-eV gate pulse. The frequency-dependent complex transmission coefficient was determined by comparing the measured terahertz electric field through the magnetite crystal to that through a reference aperture of the same size, and the complex optical parameters were then extracted numerically<sup>37</sup>.

For the ultrafast terahertz measurements, the output of the laser was split into a 1.55-eV pump beam and a terahertz probe beam, with the terahertz generation and detection scheme described above. The time delay between the pump and the probe and the time delay between the terahertz probe and the gate pulse could be varied independently. To measure the spectrally integrated response, the terahertz time was fixed at the peak of the terahertz waveform and the pump-probe delay was scanned. The spectrally resolved measurements were obtained by scanning both the terahertz time and the pump-probe delay time.

**DFT calculations.** The crystal and electronic structures of the material were optimized using the projector augmented-wave method38 within the generalized gradient approximation 39 implemented in the VASP program 40. The full relaxation of lattice parameters and atomic positions was performed in the crystallographic cell of the Cc structure containing 224 atoms. The strong electron interactions in the Fe(3d) states have been included within the local density approximation LDA + U method<sup>41</sup> with the Coulomb interaction parameter U = 4.0 eV and the Hund's exchange J = 0.8 eV. The phonon dispersion curves were obtained using the direct method<sup>42</sup> implemented in the PHONON software<sup>43</sup>. The Hellmann-Feynman forces were calculated by displacing all 56 non-equivalent atoms from their equilibrium positions along the positive and negative *x*, *y* and *z* directions, and the force-constant matrix elements were obtained. The phonon dispersions along the high-symmetry directions in the first Brillouin zone were calculated by the diagonalization of the dynamical matrix. In the Cc structure, there are 336 phonon modes at each wavevector. As discussed in the main text, Extended Data Fig. 1a shows the calculated phonon dispersion curves in the low-energy range up to 20 meV. Extended Data Fig. 1b displays the calculated partial phonon density of states projected on the Fe sites (black curve), which agrees well with experimental data taken from ref. 44 (red curve).

**Time-dependent GL calculations.** We constructed the simplest GL potential that captures phenomenologically the physics of the charge order in magnetite and is compatible with the symmetries of the system (see Supplementary Note 6). We defined the complex order parameter as  $\psi = |\psi| e^{i \varphi}$ , which is related to the real-space charge-density wave by  $\delta \rho(\mathbf{r}) = \text{Re}\{\psi e^{i \mathbf{q} \cdot \mathbf{r}}\}$ , where the wavevector could correspond to any linear combination of all the symmetry-allowed wavevectors. We modelled the transition as weakly first order, with a GL potential given by

$$F[|\psi|, \varphi] = \frac{a}{2} |\psi|^2 + \frac{b}{4} |\psi|^4 + \frac{d}{2} |\psi|^2 \sin \varphi + \frac{g}{2} \cos \varphi + F_1$$
 (1)

where  $a(T) = -A(T_{\rm V} - T)$  and  $g(T) = -G(T_{\rm V} - T)$  are functions of temperature and b > 0 for stability. A non-zero amplitude–phase interaction term d is allowed due to the lack of inversion symmetry in the low-temperature phase. The fourth term, proportional to the coefficient g, corresponds to a phenomenological 'restoring force' that could arise from a pinning potential originating in short-range impurities <sup>45–40</sup>. This term could also emerge from a linear coupling with phonon modes belonging to the same irreducible representation as the charge modulation, where the proportionality constant g would be a function of the electron–phonon coupling constant <sup>93.50</sup>. Finally, the coupling to the laser field was given by  $F_1 = E(t)^2(\eta_{\phi}|\psi|^2 + \eta_{\phi}\varphi^2)$ , where  $\eta_{\phi}$  and  $\eta_{\phi}$  are coupling constants. The pump electric field E(t) was modelled as  $E(t)^2 = 2\mathcal{F}/(c\varepsilon_0 T_p) \delta_{T_p}(t) T_p$ , where  $\mathcal{F}$  is the absorbed pump laser fluence, c is the speed of light,  $c_0$  is the permittivity of

free space,  $T_{\rm p} \approx 0.1$  ps is the pump pulse duration and  $\delta_{T_{\rm p}}(t)$  is a broadened delta function. The functional form used for the coupling to the laser field was chosen to mimic the force acting on the collective modes within the impulsive stimulated Raman scattering framework<sup>24</sup>.

Below  $T_{v_0} |\psi|^2$  acquires a finite expectation value denoted  $\psi_0$  such that  $|\psi(t)|^2 = 1 + 2\psi_0 |\delta\psi(t)| + O(\delta\psi(t)/\psi_0)^2$ . Owing to the phase–amplitude mixing allowed by the lack of inversion symmetry, the laser also couples directly to the phase  $\varphi$ . In the dynamics, we included both relaxation and inertial terms for the amplitude and phase, and we allowed them to have different relaxation rates  $\gamma_\psi$  and  $\gamma_\psi$ . The effective temperature T(t) is in general a function of time and laser fluence  $\mathcal{F}$ . However, owing to the expected slow heat diffusion, as calculated in Supplementary Note 4, we assume that it remains at its initial effective value after photoexcitation during the whole measurement,  $T(t) = T_{\rm f}$  for  $z < \lambda_p$ . The differential equations governing the system were obtained by taking the variation of the GL potential with respect to the amplitude and phase around their equilibrium positions  $\psi_0$  and  $\phi_0$ . We obtained

$$\frac{\partial^{2}|\psi|}{\partial t^{2}} + \gamma_{\psi} \frac{\partial|\psi|}{\partial t} + a(T)|\psi| + b|\psi|^{3} + d|\psi|\varphi = \eta_{\psi}E(t)^{2}\psi_{0}, \tag{2}$$

$$\frac{\partial^{2} \varphi}{\partial t^{2}} + \gamma_{\varphi} \frac{\partial \varphi}{\partial t} + d|\psi|^{2} + g(T)\varphi = \eta_{\varphi} E(t)^{2} \varphi_{0}. \tag{3}$$

We solved the coupled differential equations (2) and (3) numerically. The parameters used in Fig. 4a–d were A/b = 0.13 K<sup>-1</sup>, G/b = 0.032 K<sup>-1</sup>,  $\gamma_{\psi}/b$  = 0.5,  $\gamma_{\omega}/b$  = 0.4,  $\eta_{\omega}/\eta_{\psi}$  = 0.505 and d/b = 2.8.

## Data availability

The data that support the findings of this study are available from the corresponding author upon reasonable request.

### References

- Bałanda, M. et al. Magnetic AC susceptibility of stoichiometric and low zinc doped magnetite single crystals. Eur. Phys. J. B 43, 201–212 (2005).
- Duvillaret, L., Garet, F. & Coutaz, J.-L. A reliable method for extraction of material parameters in terahertz time-domain spectroscopy. *IEEE J. Sel. Top. Quantum Electron.* 2, 739–746 (1996).
- Blöchl, P. E. Projector augmented-wave method. *Phys. Rev. B* 50, 17953–17979 (1994).
- Perdew, J. P. et al. Restoring the density-gradient expansion for exchange in solids and surfaces. *Phys. Rev. Lett.* 100, 136406 (2008).
- Kresse, G. & Furthmüller, J. Efficient iterative schemes for *ab initio* total-energy calculations using a plane-wave basis set. *Phys. Rev. B* 54, 11169–11186 (1996).
- Liechtenstein, A. I., Anisimov, V. I. & Zaanen, J. Density-functional theory and strong interactions: orbital ordering in Mott-Hubbard insulators. *Phys. Rev. B* 52, R5467–R5470 (1995).
- 42. Parlinski, K., Li, Z. Q. & Kawazoe, Y. First-principles determination of the soft mode in cubic ZrO<sub>2</sub>. Phys. Rev. Lett. **78**, 4063–4066 (1997).
- 43. Parlinski, K. PHONON Software (Computing for Materials, 2013).
- Kołodziej, T. et al. Nuclear inelastic scattering studies of lattice dynamics in magnetite with a first- and second-order Verwey transition. *Phys. Rev. B* 85, 104301 (2012).
- Fukuyama, H. & Lee, P. A. Dynamics of the charge-density wave. I. Impurity pinning in a single chain. *Phys. Rev. B* 17, 535–541 (1978).
- Lee, P. A. & Rice, T. M. Electric field depinning of charge density waves. *Phys. Rev. B* 19, 3970–3980 (1979).
- Grüner, G. The dynamics of charge-density waves. Rev. Mod. Phys. 60, 1129–1181 (1988).
- Thomson, M. D. et al. Phase-channel dynamics reveal the role of impurities and screening in a quasi-one-dimensional charge-density wave system. Sci. Rep. 7, 2039 (2017).
- Schäfer, H., Kabanov, V. V., Beyer, M., Biljakovic, K. & Demsar, J. Disentanglement of the electronic and lattice parts of the order parameter in a 1D charge density wave system probed by femtosecond spectroscopy. *Phys. Rev. Lett.* 105, 066402 (2010).
- Schaefer, H., Kabanov, V. V. & Demsar, J. Collective modes in quasi-onedimensional charge-density wave systems probed by femtosecond timeresolved optical studies. *Phys. Rev. B* 89, 045106 (2014).

## Acknowledgements

Work at MIT was supported by the US Department of Energy, BES DMSE, Award number DE-FG02-08ER46521 and by the Gordon and Betty Moore Foundation's EPiQS Initiative grant GBMF4540. C.A.B. and E.B. acknowledge additional support from the National Science Foundation Graduate Research Fellowship under Grant No. 1122374 and the Swiss National Science Foundation under fellowships P2ELP2-172290 and P400P2-183842, respectively. M.R.-V. and G.A.F. were primarily supported under

NATURE PHYSICS LETTERS

NSF MRSEC award DMR-1720595. G.A.F also acknowledges support from a Simons Fellowship. A.M.O. is grateful for the Alexander von Humboldt Foundation Fellowship (Humboldt-Forschungspreis). A.M.O. and P.P. acknowledge the support of Narodowe Centrum Nauki (NCN, National Science Centre, Poland), Projects No. 2016/23/B/ST3/00839 and No. 2017/25/B/ST3/02586, respectively. D.L. acknowledges the project IT4Innovations National Supercomputing Center CZ.02.1.01/0.0/0.0/ 16\_013/0001791 and Grant No. 17-27790S of the Grant Agency of the Czech Republic. J.L. acknowledges financial support from Italian MAECI through the collaborative project SUPERTOP-PGR04879, bilateral project AR17MO7, Italian MIUR under the PRIN project Quantum2D, Grant No. 2017Z8TS5B, and from Regione Lazio (L.R. 13/08) under project SIMAP.

### **Author contributions**

E.B. conceived the study. C.A.B., E.B. and I.O.O. performed the experiments. C.A.B. and E.B. analysed the experimental data. A.K. grew the magnetite single crystals. P.P., D.L., K.P. and A.M.O. performed the DFT calculations. M.R.-V. and G.A.F. performed the time-dependent GL calculations. J.L. developed the model of coherent polaron

tunnelling with input from P.P. and contributed to the data interpretation. C.A.B., E.B. and N.G. wrote the manuscript with crucial input from all other authors. This project was supervised by N.G.

## **Competing interests**

The authors declare no competing interests.

#### Additional information

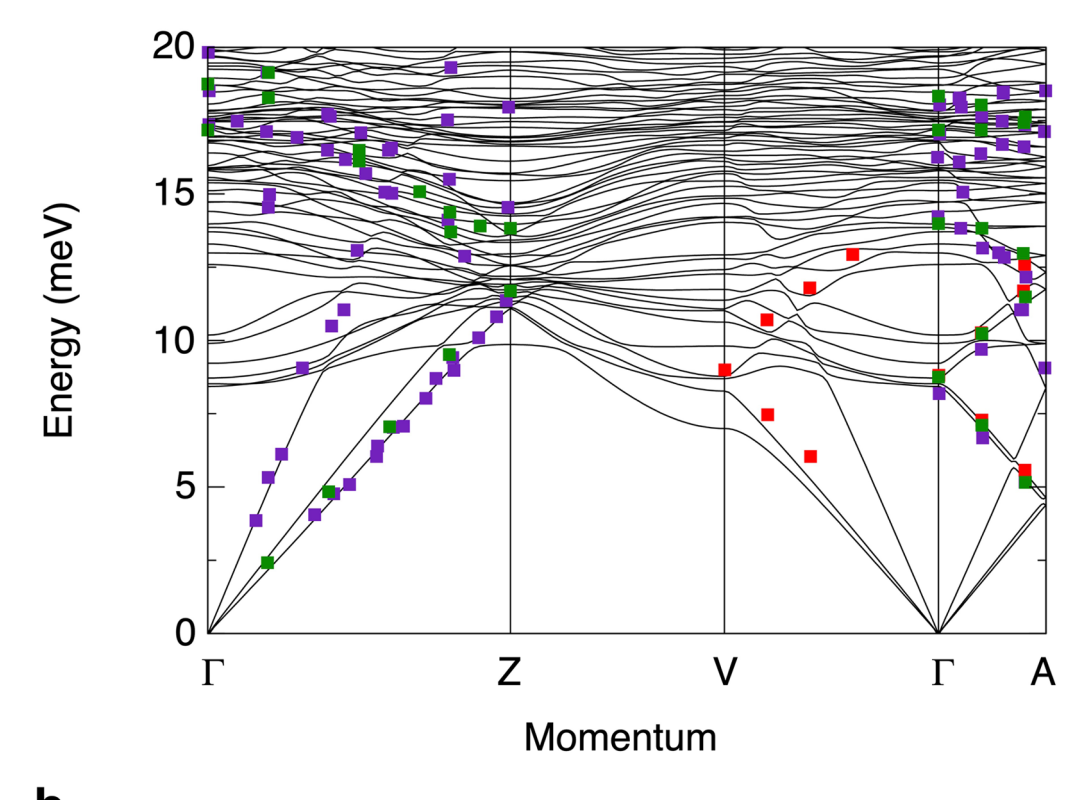
**Extended data** is available for this paper at https://doi.org/10.1038/s41567-020-0823-y. **Supplementary information** is available for this paper at https://doi.org/10.1038/s41567-020-0823-y.

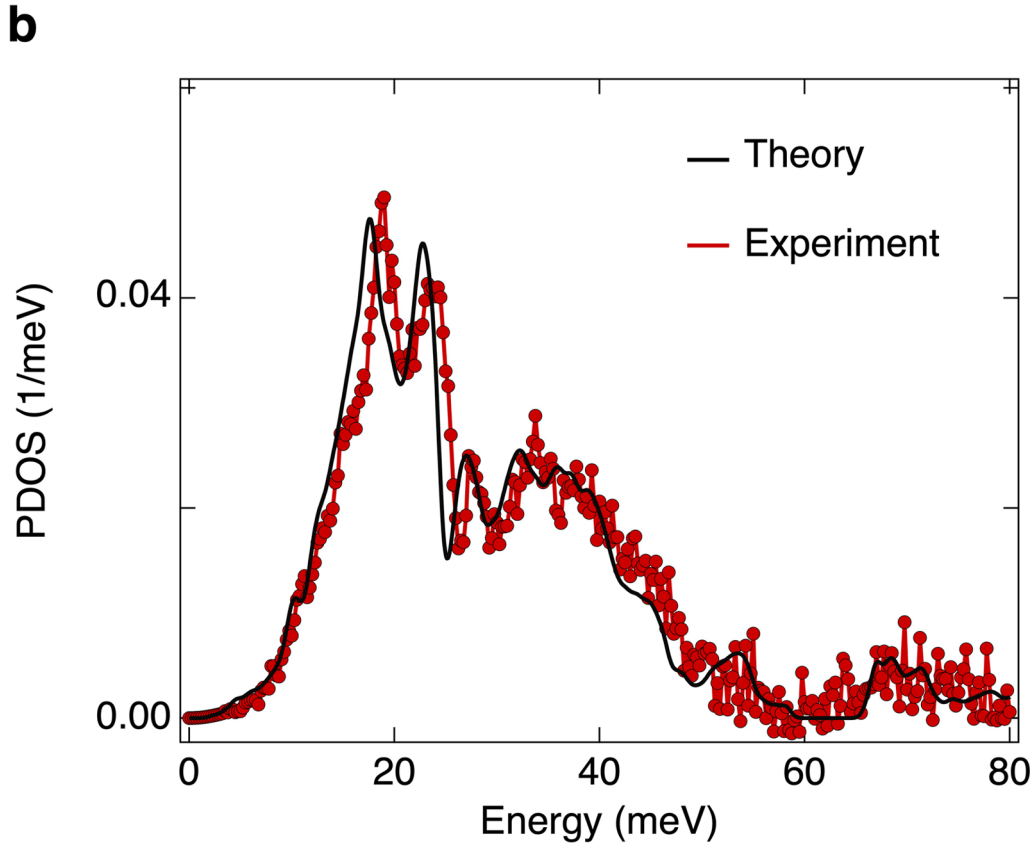
Correspondence and requests for materials should be addressed to N.G.

**Peer review information** *Nature Physics* thanks Fulvio Parmigiani and the other, anonymous, reviewer(s) for their contribution to the peer review of this work.

Reprints and permissions information is available at www.nature.com/reprints.

a





**Extended Data Fig. 1 DFT calculation of the phonon dispersion in the** *Cc* **structure. <b>a**, Low-energy phonon energy-momentum dispersion curves of magnetite calculated for the monoclinic *Cc* symmetry. The symbols mark the energies of the phonon modes measured experimentally by inelastic neutron scattering (violet symbols from ref.  $^{23}$  and red symbols from ref.  $^{19}$ ) and inelastic x-ray scattering (green symbols from ref.  $^{12}$ ). There are no optical phonon branches in the energy range of the two newly-observed collective modes (1 – 4 meV). **b**, Partial phonon density of states projected on the Fe sites. The results of the DFT calculations are shown in black, while the experimental results at 50 K (taken from ref.  $^{44}$ ) are in red.